Petroleum Science 23 (2026) 5610–5623

Contents lists available at ScienceDirect

Petroleum Science

journal homepage: www.keaipublishing.com/en/journals/petroleum-science

Original Paper

Investigation on force responses in ridged diamond element breaking granite

Chao Xiong [a,b,c,*], Xin-Long Li [c], Sen-Lin He [c], Zhong-Wei Huang [a,c,**], Huai-Zhong Shi [c], Wen-Hao He [a,c]

[a] State Key Laboratory of Deep Geothermal Resources, Beijing, 102249, China
[b] Center of Advanced Oil and Gas Equipment, China University of Petroleum (Beijing), Beijing, 102249, China
[c] State Key Laboratory of Petroleum Resources and Engineering, China University of Petroleum (Beijing), Beijing, 102249, China

A R T I C L E I N F O

Article history:
Received 14 May 2025
Received in revised form
1 April 2026
Accepted 18 May 2026
Available online 9 June 2026

Edited by Jia-Jia Fei

Keywords:
Ridged diamond element
Force response
Mechanical model
Single cutter test

A B S T R A C T

Ridged diamond element (RDE), a new 3D shaped PDC cutter, has higher impact and wear resistance than conventional plane PDC cutter. Furthermore, RDE also can significantly improve the rock-breaking efficiency of PDC drill bits in hard rock. The investigation on force response during the RDE breaking rock is a critically important work for revealing the rock breakage mechanism and designing the Axe-Blade PDC bit. However, to our best knowledge, there is still a lack of systematic and in-depth research on the force response of RDE cutting hard rock. This paper conducted a series of single cutter tests on granite, and measured the triaxial forces of RDE under different depth of cut (DOC) and back rake angle. Then, a mechanical model of interaction between RDE and rock was established through theoretical derivation. The model accuracy is validated by experimental data, and the average error of prediction cutting force and normal force is 3.13% and 3.68% respectively. Lastly, the influence of DOC, back rake angle, cutter diameter and ridge angle on cutting force and normal force was analyzed, and the influence weights of four parameters were revealed by random forest method. The results show that the cutting force and the normal force increase with DOC in a quadratic polynomial relationship. With the increase in back rake angle, cutter diameter and ridge angle, the cutting force and normal force show an increasing trend, but there are significant differences in the rate of increase. When the back rake angle increases from 10° to 30° for DOC of 2 mm, the cutting force and normal force increases by 416.22 and 1008.04 N respectively. The cutter diameter increases from 10 to 20 mm, the cutting force and normal force increases by 1318.13 and 1739.10 N respectively. The ridge angle increases from 100° to 165°, the cutting force and normal force increases by 1276.03 and 750.87 N respectively. The DOC has the largest influence weight on the force response of RDE in four parameters. The findings of this work can provide theoretical guidance for the cutter arrangement of AxeBlade PDC bit.

1. Introduction

Polycrystalline diamond compact (PDC) bits have been widely used in oil and gas drilling due to their high rate of penetration (ROP) and long life (Bellin et al., 2010; Miyazaki et al., 2019). However, PDC bits are sensitive to the properties of formation rock. Conventional PDC cutters are usually suitable for drilling in homogeneous rock from soft to medium-hard but cannot effectively drill hard rock (Che and Ehmann, 2014). In recent ten years, the geometry of PDC cutter is changing from conventional planar to three-dimensional (3D) shape, and many 3D shaped cutters are invented (Xiong et al., 2020a; Zhu et al., 2022). The impact and wear resistance of 3D shaped cutter have been significantly increased. The PDC bit using 3D shaped cutters demonstrate excellent rock breaking and durability in hard and multi-interbedded formation (Shao et al., 2021; Shi et al., 2026; Xiong et al., 2020b).

Ridged diamond element (RDE) is a typical 3D cutter as shown in Fig. 1(a). It cuts rock with an innovative way (Fig. 1(b)), which combines the shearing action of a conventional PDC cutter with the crushing action of a tungsten carbide insert (TCI), achieving at

* Corresponding author.
** Corresponding author.
E-mail addresses: xiongc@cup.edu.cn (C. Xiong), huangzw@cup.edu.cn (Z.-W. Huang).
Peer review under the responsibility of China University of Petroleum (Beijing).

https://doi.org/10.1016/j.petsci.2026.05.026

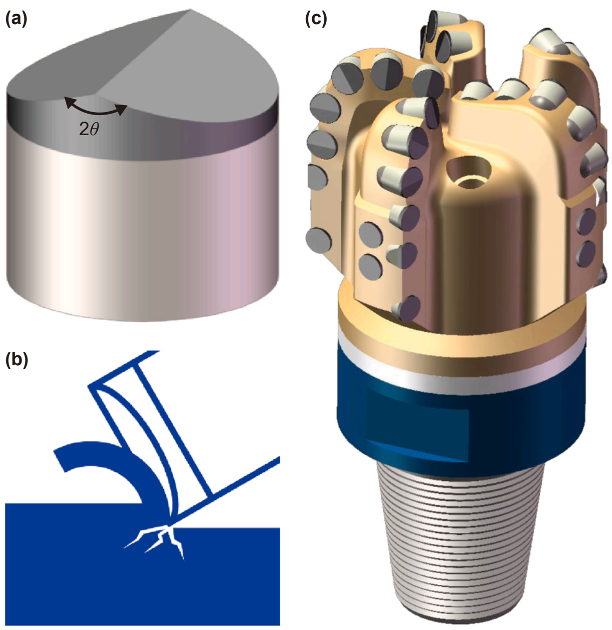

Fig. 1. (**a**) RDE, (**b**) diagram of RDE breaking rock and (**c**) AxeBlade PDC bit.

least 22% deeper penetration to provide higher instantaneous ROP using the same weight on bit (WOB) and revolutions per minute (RPM) applied to conventional PDC cutters (Lomov et al., 2018). The diamond table on the RDE ridge is 70% thicker than that of a conventional cutter, which gives the RDE even more strength and resistance to impact and wear (Gumich et al., 2017; Negm et al., 2016). Thus, the AxeBlade PDC bit, as shown in Fig. 1(c), installed RDE can deliver improved durability and dull condition for maximum ROP throughout the run. Field performance of the AxeBlade PDC bit demonstrates up to 29% improvement in ROP for hard and brittle formations compared with similar bit designs using conventional PDC cutters (Schlumberger, 2026).

Since the invention of RDE, many researchers have conducted a series of laboratory tests and numerical modeling for RDE breaking rock. Crane et al. (2017) conducted a single-cutter test for the RDE and conventional PDC cutter. It was found that cutting forces and normal forces recorded on the RDE are about 40% less than that of a conventional PDC cutter. Lin et al. (2019) studied the rock breaking process of the RDE through experiments and numerical simulation. The influence of ridge angle, back rake angle, side rake angle, penetration depth, and cutter rotation angle on rock-breaking efficiency were analyzed. Zou et al. (2021b) compared the characteristics of conventional PDC cutter and RDE breaking silica dolomite. The results show that under the same WOB, RDE penetrate deeper into the rock and cutting force is 61.54% smaller than that of conventional PDC cutter. Based on ABAQUS software, former researchers analyzed the characteristics of RDE breaking rock, and studied the effect of rock-mechanical parameters, cutting parameters and cutter geometrical parameters on the cutting force and rock breaking efficiency (Gong et al., 2022; Zhao et al., 2021; Zou et al., 2021a). Liu et al. (2022) investigated the formation process of cuttings during the RDE breaking rock through experiments, and analyzed the influences of depth of cut (DOC) and back rake angle on the mass fraction and particle size distribution of cuttings. Through experiments and numerical simulation, Zou et al. (2022) revealed the rock breaking mechanism of RDE. The rock at the tip of the cutter forms a localized area of high shear stress concentration, leading to shear failure of the rock. When the RDE penetrates into the rock, it induces tensile failure on its sides. Shao et al. (2021) compared the different rock-breaking mechanisms between RDE and conventional PDC cutter through single-cutter test. The results show that the cutting force and normal force linearly increase with the increasing of DOC.

Even though numerous researches studied the rock breaking efficiency and process, the researches on the force response of RDE breaking rock are still limited. Force response prediction is considered as the most straightforward method of indicating the performance of the PDC cutters (Gerbaud et al., 2006). Moreover, the force response model of a single PDC cutter can be used for predicting the resultant forces that act on the whole PDC bit by integration of the force responses of the single cutters over the whole body of the PDC bits (Chen et al., 2021; Glowka, 1989). Nishimatsu (1972) established a cutting force model of a wedge-shaped cutter based on the Mohr failure criterion and rock stress analysis. Che and Ehmann (2014) established a phenomenological force response model for conventional PDC cutter based on the experimental data and the physics at rock-cutter interface. Chen et al. (2018) developed a 2D cutting model of single conventional PDC cutter based on the linear poroelasticity theory. Cheng et al. (2019) proposed a 2D cutting force model of single conventional PDC cutter with the assumption that the rock was a semi-infinite elastic plastic planar body. Li et al. (2020) developed a single conventional PDC cutter force model by modifying the Nishimatsu model. Xiong et al. (2021) developed a 3D cutting force model of a stinger PDC cutter based on rock stress analysis by assuming the rock as a semi-infinite elastic body. In a word, the majority of existing force response models are suitable for conventional PDC cutter. However, it is important to note that the rock breaking mechanism and force response by RDE differ significantly from those of conventional PDC cutter. Consequently, the application of conventional PDC cutter force response models is unsuitable for RDE. To our best knowledge, the force response model of RDE is still masked.

The objective of this paper is to research the force response of RDE breaking granite and develop a force model of RDE for the PDC bit designment. Firstly, the experiment of single cutter tests for RDE breaking granite is carried out, and the triaxial forces response of RDE breaking rock under different DOC and back rake angle are measured. Then, based on the analysis of the geometric characteristics and force characteristics of RDE, the mechanical model of interaction between RDE and rock is established through theoretical derivation, and the parameter calibration and accuracy verification of the model are carried out through the experimental data. Finally, based on the established theoretical model, the influence of DOC, back rake angle, cutter diameter and ridge angle on cutting force and normal force is analyzed, and the influence weights of four parameters on the cutting force and normal force are revealed by random forest method.

2. Experimental research

2.1. Experimental apparatus

The experimental equipment was developed on a single column vertical lathe, as shown in Fig. 2, which is composed of the cutting system and measurement/control system. It can be used to conduct straight line cutting and rotary cutting experiment. The cutting system is mainly consisted of rotating platform, rock clamping device, PDC cutter, tool holder and triaxial forces sensor. The rotational speed of rotating platform can be set to 38, 65, 76, 85, 130, 150, 170 and 300 rpm. The maximum 500 mm cube rock sample and cylindrical rock sample with diameter of 750 mm and height of 500 mm can be used to carry out the cutting experiment. The back rake angle of PDC cutter can be adjusted in the range of

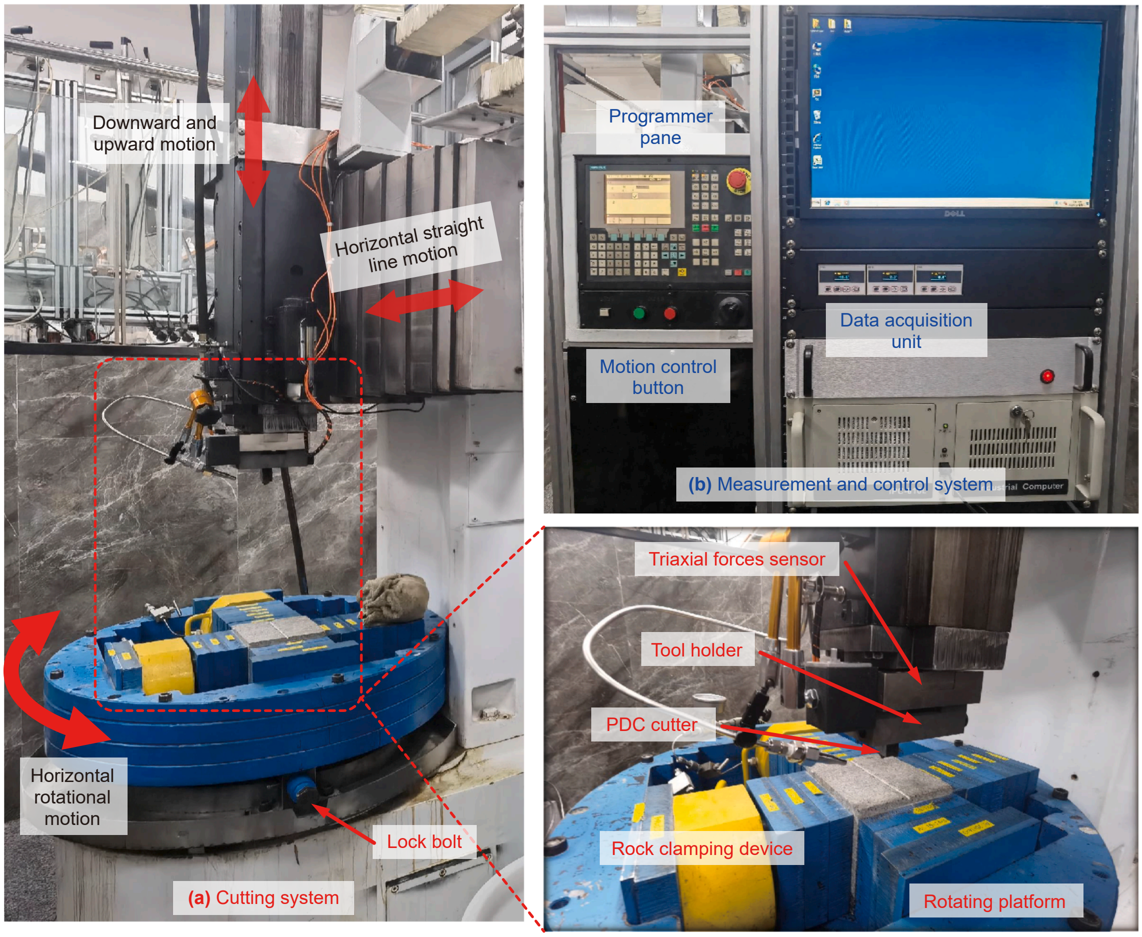

Fig. 2. Experimental setup for RDE breaking granite.

0°–50°. A DYDW-005 multi-dimensional force sensor is installed above the tool holder to measure the force response of the cutter in *x*, *y*, and *z* directions during the cutting process. The measurement range of the triaxial forces sensor is 0−10 kN, and the response frequency is 10 kHz. The measurement/control system includes programmer pane, motion control button and data acquisition unit. Through the programmer pane, code can be written to control the DOC, cutting speed and cutting mode (linear cutting and rotary cutting) during the experiment. Signal acquisition is realized through LabVIEW USB 3210 with a DECENT company data acquisition system. The maximum sample rates are 3200 Hz.

2.2. Cutter and rock materials

The RDE cutter used in this experiment is shown in Fig. 3(a). A 3D Profilometer, as shown in Fig. 3(b), was used to measure the geometrical parameters of RDE cutter. Fig. 3(c–e) are the measurement results of RDE's ridge angle and diameter in this work. The RDE has a 164.44° ridge angle and 16 mm diameter.

The granite specimens utilized in this study were sourced from natural outcrops in Shandong Province, China. X-ray diffraction (XRD) analysis revealed that the mineralogical composition consists predominantly of *K*-feldspar (38.3%) and plagioclase (29.9%). In addition, as shown in Fig. 4(a) and (b), the physical and mechanical properties were systematically characterized using an RTR-1500 HTHP rock triaxial testing system. The uniaxial compressive strength (UCS) of granite is 129.78 MPa, and its Young's modulus is 41.30 GPa. The other parameters are shown in our previous article (Xiong et al., 2023a). Prior to experimental testing, intact granite blocks free from macroscopic fractures or structural defects were selected and machined into cubic specimens measuring 150 × 150 × 150 mm^3 shown in Fig. 4(c).

2.3. Experimental procedures

As shown in Fig. 5, the straight-line cutting experiment was carried out in this study. The rock sample remains stationary, and the RDE cutter moved in a straight line with the speed of 25 mm/s to cut the rock. In this paper, 25 experimental scenarios were designed under different DOC and back rake angle (α). The DOC is set to five levels, i.e., 1.0, 1.5, 2.0, 2.5, and 3.0 mm. The back rake angle is set to five levels, i.e., 10°, 15°, 20°, 25°, and 30°.

During the cutting process, the DOC should be kept constant. So, before the experiment, the rock surfaces were finished with high-precision machine tools to ensure flatness. The flatness of cutting surface is controlled within 0.05 mm. The experimental procedure is as follows: (1) put the prepared granite sample on the rotating platform, and use the rock clamping device to fix the rock sample; (2) put the RDE cutter on the tool holder, adjust the back rake angle and lock it, then hold the rotating platform stationary through lock bolt; (3) write code on the programmer pane to set the DOC, cutting speed and cutting distance (170 mm); (4) open data acquisition and control software, push the motion control button and begin the cutting experiment. The force in *x*, *y*, and *z* directions was measured and recorded with a sample rate of 200 points/s during the whole cutting period; (5) after the cutting tests, open the rock clamping device, take out the granite sample, and one cutting test is finished.

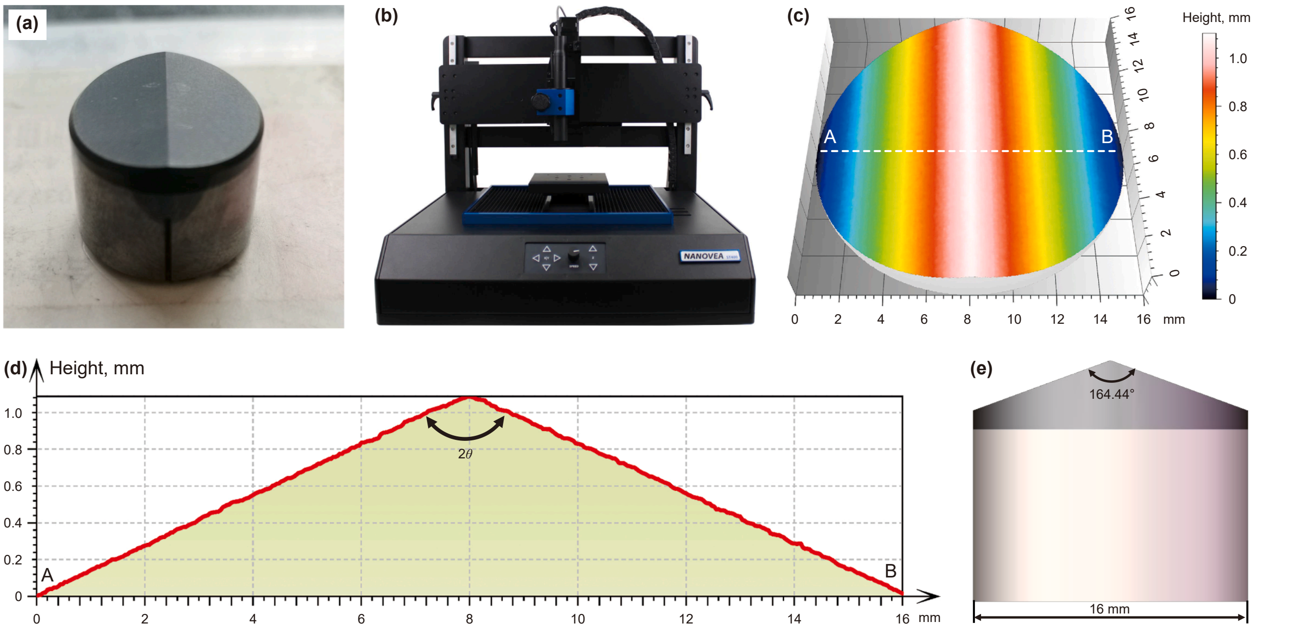

Fig. 3. (**a**) The RDE used in the experiment; (**b**) ST400 3D Profilometer; (**c**–**e**) Measurement and results of geometric parameters of RDE.

2.4. Experimental results

Fig. 6 displays experimental data depicting force responses in relation to cutting time during the RDE cutter breaking granite. The cutting parameters include a DOC of 2 mm and a back rake angle of 20°. It presents that the force has significant fluctuation, especially for the cutting force and normal force, which is due to the brittle fracture characteristics and the inhomogeneous microstructure of the rock (Che et al., 2017; Dai et al., 2023; Fu et al., 2025). The cutting force and normal force repeat a process: gradually increasing, reaching a peak, and then rapidly decreasing. In addition, it is interesting to observe that the cutting force and normal force fluctuates at the same pace, but their amplitude is not the same. The average value is considered as a good representative of the dynamic force responses in single cutter tests (Che et al., 2017; Xiong et al., 2023b). In this paper, the cutting force and normal force at the stable phase with the cutting

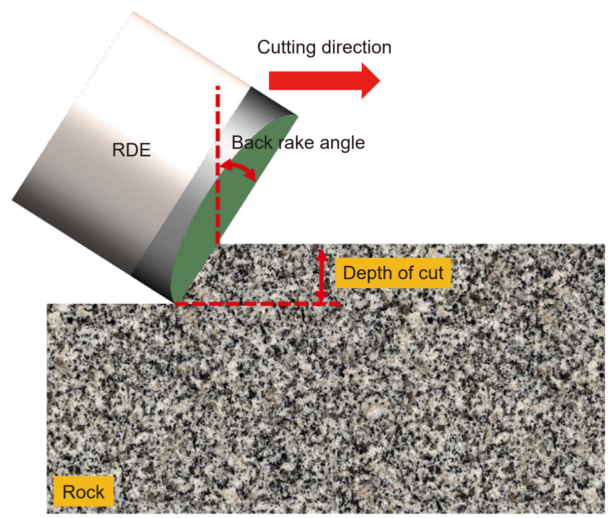

Fig. 5. Diagram of rock breaking by straight line cutting with RDE.

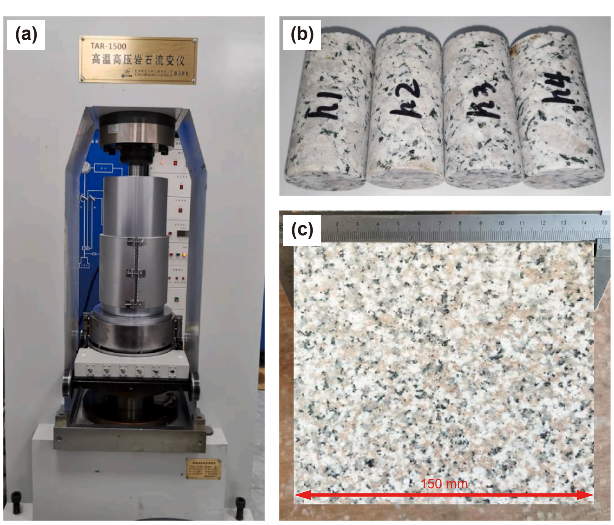

Fig. 4. (**a**) RTR-1500 HTHP rock triaxial apparatus; (**b**) The cylindrical rock sample with a diameter of 50 mm and a height of 100 mm for testing rock mechanics parameters; (**c**) Sample size of granite used in this experiment.

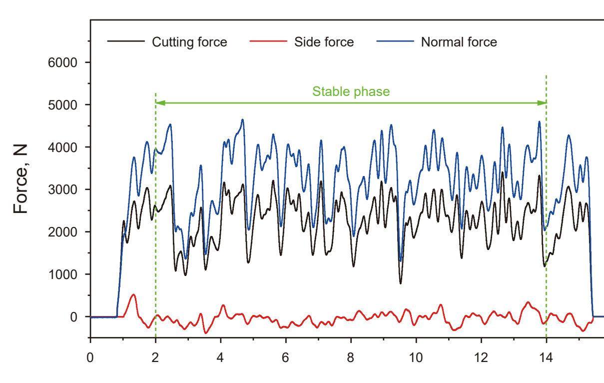

Fig. 6. The experimental data of force responses with cutting time (DOC = 2 mm and $\alpha = 20°$).

Table 1
Experimental results.

No.	α, °	DOC, mm	Cutting force, N	Normal force, N
1	10	1.0	1222.33	1737.15
2		1.5	1669.77	2391.91
3		2.0	2057.53	2998.11
4		2.5	2682.19	3523.88
5		3.0	3173.94	4155.32
6	15	1.0	1355.68	1958.22
7		1.5	1868.05	2565.13
8		2.0	2265.88	3183.71
9		2.5	2808.30	3861.24
10		3.0	3292.25	4472.11
11	20	1.0	1446.61	2147.82
12		1.5	1881.29	2754.27
13		2.0	2284.45	3397.46
14		2.5	2907.96	4258.16
15		3.0	3462.20	4870.95
16	25	1.0	1540.62	2425.21
17		1.5	1923.59	2910.54
18		2.0	2400.86	3608.03
19		2.5	3062.70	4518.05
20		3.0	3596.73	5264.25
21	30	1.0	1648.64	2618.15
22		1.5	2056.42	3211.11
23		2.0	2536.02	3950.44
24		2.5	3167.25	4758.08
25		3.0	3792.67	5531.25

time ranging from 2 to 14 s are selected to calculate the average value to decrease the error caused by the boundary effects (Xiong et al., 2020a, 2023a). The experimental data is processed using the above method and the results are shown in Table 1. The side force fluctuates around 0 N, which is due to the symmetric geometry structure and loading of RDE cutter.

3. Mechanical model of RDE–rock interaction

In this section, firstly considering the three-dimensional cutting structure of RDE, the force response analysis of RDE breaking rock is carried out. Then, the mechanical model of interaction between RDE and rock is established through theoretical derivation. Lastly, the unknown parameters in the theoretical model are determined through regression analysis of experimental data.

3.1. Theoretical model derivation

Fig. 7 shows the schematic diagram of a RDE cutting rock. During the cutting process, there are two kind forces applied by RDE on the rock, namely contact force N and friction force S. From a physical perspective, N is generated due to the squeezing action of cutter, which along the outward normal of the contact surface, while S is generated due to the frictional action between the rock and cutter, whose direction is vertical to the contact force N and lies within the plane surface I. The friction force S can be decomposed into force S_1 and force S_2. Force S_1 is parallel to ridge line 1, and force S_2 is parallel to the upper surface of the rock. Both of them are located within plane surface I. As shown in Fig. 7, the Cartesian coordinate system is established. The X-axis direction represents the cutting direction, while the Z-axis direction is oriented vertically upward from the rock surface. Consequently, contact force N and friction force S_1 and S_2 can be decomposed along the coordinate axes.

Fig. 8 shows the schematic diagram of force decomposition for S_1 and S_2. The friction force S_1 can be decomposed along the X-axis and Z-axis. The friction force S_2 can be decomposed along the X-axis and Y-axis.

$$S_{1x} = -S_1 \cdot \sin\alpha \tag{1}$$

$$S_{1z} = -S_1 \cdot \cos\alpha \tag{2}$$

$$S_{2x} = S_2 \cdot \sin\beta \tag{3}$$

$$S_{2y} = -S_2 \cdot \cos\beta \tag{4}$$

where, α is the back rake angle, β is the angle between the friction force S_2 and the negative direction of Y-axis.

Fig. 9 presents the schematic diagram of angle β. Plane 1 represents the surface of rock. Plane 2 is formed by rotating Plane 1 around the Y-axis by an angle of α. Plane 3 is the symmetrical plane of the RDE, where the line OE coincides with the ridge line of the RDE. Plane 4 coincides with the plane surface I of RDE. Take point A on the intersection of plane 2 and plane 3, and make the perpendicular line of plane 3 from point A, and the perpendicular foot is point D. In plane 3, the perpendicular line of line OD is made from point D, which intersects plane 1 at point C. In plane 1, crossing point C is the perpendicular line of OC, which intersects plane 4 at point B. According to the geometrical relationships, $\angle BOF$ is angle β. $\angle AOD$ is half of the axe shape angel of the RDE, denoted as angle θ. $\angle DOC$ is the back rake angle α.

As shown in Fig. 9, according to the geometrical relationships: $AD \perp OD$, $DC \perp OD$, $OC \perp CB$, the following relationship can be obtained:

$$\overline{AB} = \overline{CD} = \overline{OA} \cdot \cos\theta \cdot \tan\alpha \tag{5}$$

$$\overline{OB} = \overline{OA} \cdot \cos\theta / (\cos\alpha \cdot \sin\beta) \tag{6}$$

$$\angle BAO = \frac{\pi}{2} \tag{7}$$

Thus, $\overline{OB}^2 = \overline{OA}^2 + \overline{AB}^2$, and according to Eqs. (5)–(7), $\sin\beta$ can be express as:

$$\sin\beta = \sqrt{\frac{\cos^2\theta}{\cos^2\alpha + \cos^2\theta \cdot \sin^2\alpha}} \tag{8}$$

In the $OXYZ$ Cartesian coordinate system in Fig. 9, if the length of line OE is equal to m and the length of line OB is equal to n, the coordinates of point E are $(m \cdot \sin\alpha, 0, m \cdot \cos\alpha)$, and the coordinates of point B are $(-n \cdot \sin\beta, n \cdot \cos\beta, 0)$. Then, the vector $\overrightarrow{OB} = (-n \cdot \sin\beta, n \cdot \cos\beta, 0)$ and vector $\overrightarrow{OE} = (m \cdot \sin\alpha, 0, m \cdot \cos\alpha)$. The contact force N is perpendicular to plane 4. The unit vector $\overrightarrow{n}$ in the same direction as the contact force N can be represented as:

$$\overrightarrow{n} = \frac{\overrightarrow{OB} \times \overrightarrow{OE}}{\left|\overrightarrow{OB} \times \overrightarrow{OE}\right|} = \left(\frac{\cos\beta \cdot \cos\alpha}{\sqrt{\cos^2\alpha + \cos^2\beta \cdot \sin^2\alpha}}\right)\overrightarrow{i} + \left(\frac{\sin\beta \cdot \cos\alpha}{\sqrt{\cos^2\alpha + \cos^2\beta \cdot \sin^2\alpha}}\right)\overrightarrow{j} + \left(\frac{-\cos\beta \cdot \sin\alpha}{\sqrt{\cos^2\alpha + \cos^2\beta \cdot \sin^2\alpha}}\right)\overrightarrow{k} \tag{9}$$

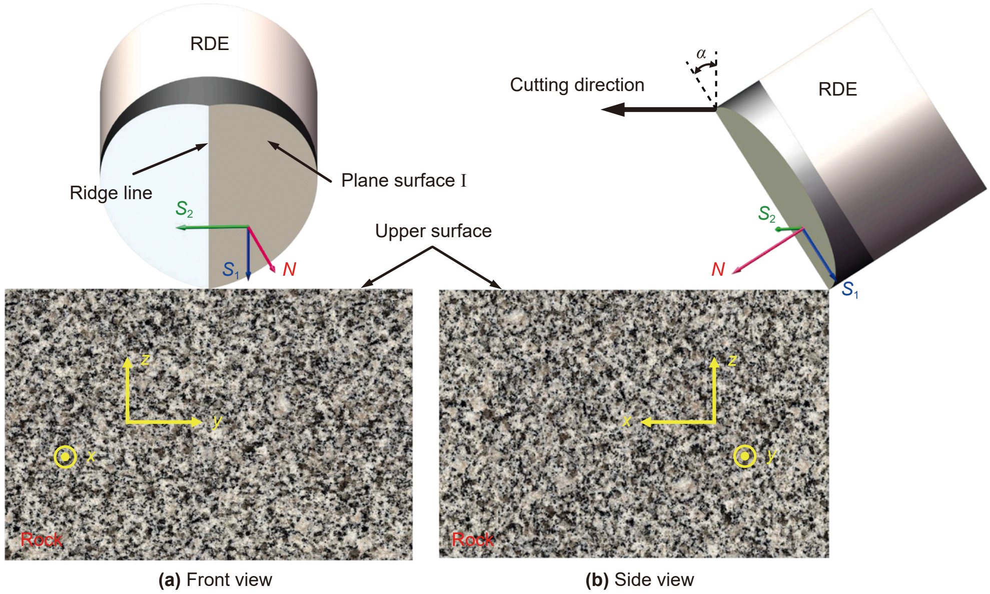

Fig. 7. Schematic diagram of force response of RDE cutting rock.

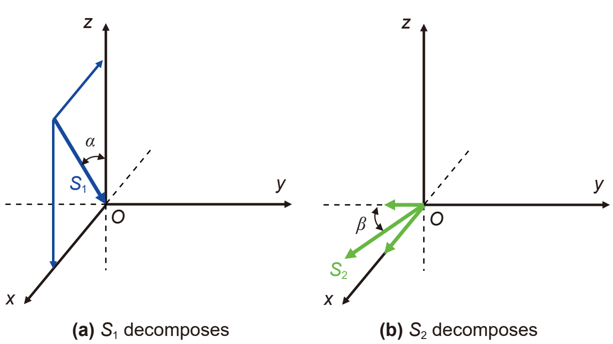

Fig. 8. Schematic diagram of friction force decomposition.

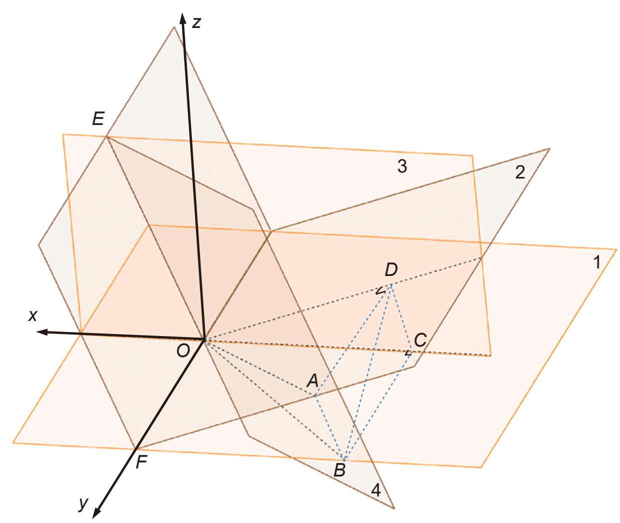

Fig. 9. Schematic diagram of angle β

Substitute Eq. (8) into Eq. (9), the unit vector $\vec{n}$ can be expressed as:

$$\vec{n} = \sin\theta\cdot\cos\alpha\cdot\vec{i} + \cos\theta\cdot\vec{j} + (-\sin\theta\cdot\sin\alpha)\cdot\vec{k} \tag{10}$$

Therefore, the contact force N can be decomposed into three component forces along the X, Y, and Z directions:

$$N_x = \sin\theta\cdot\cos\alpha\cdot N \tag{11}$$

$$N_y = \cos\theta\cdot N \tag{12}$$

$$N_z = -\sin\theta\cdot\sin\alpha\cdot N \tag{13}$$

Based on the symmetrical structure of the RDE, according to Eqs. (1)–(4), (11)–(13), the RDE–rock interaction force can be decomposed into three component forces along the X, Y, and Z directions:

$$\begin{aligned} F_x &= 2(S_{1x}+S_{2x}+N_x) = -2S_1\cdot\sin\alpha + 2S_2\cdot\sin\beta + 2N\sin\theta\cdot\cos\alpha \\ F_y &= 0 \\ F_z &= 2(S_{1z}+N_z) = -2S_1\cdot\cos\alpha - 2N\cdot\sin\theta\cdot\sin\alpha \end{aligned} \tag{14}$$

During the cutting process, a force F is imparted by the RDE onto the rock, let F_c and F_n denote the force components that are parallel and normal to the rock surface, named cutting force and normal force respectively. Thus, according to Eq. (14), the cutting force F_c and normal force F_n can be expressed as:

$$\begin{aligned} F_c &= -2S_1\cdot\sin\alpha + 2S_2\cdot\sin\beta + 2N\cdot\sin\theta\cdot\cos\alpha \\ F_n &= 2S_1\cdot\cos\alpha + 2N\cdot\sin\theta\cdot\sin\alpha \end{aligned} \tag{15}$$

3.2. Model parameters determination

As we all know, the contact force N and friction force S can be related by the friction coefficient. Thus, Eq. (15) can be expressed as:

$$\begin{aligned} F_c &= -2N\cdot\mu_1\cdot\sin\alpha + 2N\cdot\mu_2\cdot\sin\beta + 2N\cdot\sin\theta\cdot\cos\alpha \\ F_n &= 2N\cdot\mu_1\cdot\cos\alpha + 2N\cdot\sin\theta\cdot\sin\alpha \end{aligned} \tag{16}$$

where, μ_1 and μ_2 are the friction coefficient.

If $w = F_c/F_n$, the following equation can be derived according to Eq. (16):

$$(w\cdot\cos\alpha + \sin\alpha)\cdot\mu_1 - \sin\beta\cdot\mu_2 = \sin\theta(\cos\alpha - w\cdot\sin\alpha) \tag{17}$$

As described in Section 2, the ridge angle (2θ) is 164.44°. The back rake angle (α) varies within the range of 10°–30°. Based on the experimental results in Table 1, $\mu_1 = 0.7$ and $\mu_2 \approx 0$ can be obtained by least square fitting according to Eq. (17). This implies that the frictional force S_2 is very small relative to the frictional force S_1. Therefore, we can ignore the part containing S_2 in Eq. (15), and obtain the new expressions for the cutting force F_c and normal force F_n as follows:

$$\begin{aligned} F_c &= -2S_1\cdot\sin\alpha + 2N\cdot\sin\theta\cdot\cos\alpha \\ F_n &= 2S_1\cdot\cos\alpha + 2N\cdot\sin\theta\cdot\sin\alpha \end{aligned} \tag{18}$$

Thus, the contact force N and friction force S_1 can be expressed as:

$$\begin{aligned} N &= \frac{F_c\cdot\cos\alpha + F_n\cdot\sin\alpha}{2\ \sin\theta} \\ S_1 &= \frac{F_n\cdot\cos\alpha - F_c\cdot\sin\alpha}{2} \end{aligned} \tag{19}$$

Using the experimentally measured cutting force F_c and normal force F_n shown in Table 1 and substituting them into Eq. (19), the contact force N and friction force S_1 can be calculated. In addition, the contact force N and friction force S_1 are formed on the contact surface between RDE and rock as shown in Fig. 7. The geometric properties of the contact surface will directly influence the contact force N and friction force S_1, thereby affecting the force on the RDE cutter. Ma and Wang (2006) have demonstrated through experiments that the contact area and contact arc length are the primary geometric parameters influencing the force on the cutter, and the force exhibits a linear relationship with the product of contact area and contact arc length when the back rake angle is constant. Fig. 10 presents the schematic diagram of contact area and contact arc length. It is clearly shown that $2S_{AQO}$ is the contact area and $2\widehat{OA}$ is the contact arc length.

As shown in Fig. 10, the plane surface I of the RDE cutter is a semi-ellipse. It can be expressed by:

$$\frac{x^2}{a^2} + \frac{y^2}{b^2} = 1\ (a > b > 0) \tag{20}$$

where a is equal to $\frac{r}{\sin\theta}$ and b is equal to r. θ is half of the axe shape angel of the RDE. r is the radius of the RDE cutter. According to the geometrical relationships, $\angle AQK = \beta$, $\angle OQG = \alpha$. A Cartesian coordinate system is established as shown in Fig. 9, the vector $\overrightarrow{OB} = (-n\cdot\sin\beta, n\cdot\cos\beta, 0)$ and vector $\overrightarrow{OE} = (m\cdot\sin\alpha, 0, m\cdot\cos\alpha)$, thus γ can be expressed as:

$$\cos(\pi - \gamma) = -\cos\gamma = \frac{\overrightarrow{OB}\cdot\overrightarrow{OE}}{\left|\overrightarrow{OB}\right|\cdot\left|\overrightarrow{OE}\right|} = -\sin\beta\cdot\sin\alpha \tag{21}$$

The equation for the line AQ can be expressed as:

$$y = k_0\cdot x + m_0 \tag{22}$$

where k_0 is equal to $-1/\tan\gamma$ and m_0 is equal to $h/\cos\alpha - r$, h is the DOC.

In order to obtain the coordinates of point A (x_0, y_0), substitute Eq. (22) into Eq. (20), we can get:

$$\left(b^2 + a^2{k_0}^2\right)x^2 + 2a^2k_0m_0x + a^2\left({m_0}^2 - b^2\right) = 0 \tag{23}$$

According to the root formula of the quadratic equation of one variable, we can get:

$$x_0 = \frac{-a^2k_0m_0 + ab\sqrt{b^2 + a^2{k_0}^2 - {m_0}^2}}{b^2 + a^2{k_0}^2} \tag{24}$$

Substitute Eq. (24) into Eq. (22), we can get:

$$y_0 = \frac{-a^2{k_0}^2m_0 + abk_0\sqrt{b^2 + a^2{k_0}^2 - {m_0}^2}}{b^2 + a^2{k_0}^2} + m_0 \tag{25}$$

The contact area $2S_{AQO}$ can be expressed as:

$$\begin{aligned} 2S_{AQO} &= 2\int_0^{x_0}\sqrt{b^2 - \frac{b^2}{a^2}\cdot x^2}\mathrm{d}x - (-m_0 - y_0)x_0 = 2\frac{b}{a} \\ &\left(\frac{x_0}{2}\sqrt{a^2 - x_0^2} + \frac{a^2}{2}\arcsin\frac{x_0}{a}\right) + (m_0 + y_0)x_0 \end{aligned} \tag{26}$$

The contact arc length $2\widehat{OA}$ can be expressed as:

$$2\widehat{OA} = 2\int_0^{x_0}\sqrt{\mathrm{d}x^2 + \mathrm{d}y^2} = 2\int_0^{x_0}\sqrt{\frac{a^4 + \left(b^2 - a^2\right)\cdot x^2}{a^4 - a^2\cdot x^2}}\mathrm{d}x \tag{27}$$

It can be found that the integrand in Eq. (27) is a function without an elementary antiderivative. Hence, we use the fundamental theorem of calculus to compute the integral Eq. (27) by programming. As described in Section 2, the diameter ($2r$) of the RDE is 16 mm and the ridge angle (2θ) is 164.44°. The back rake angle (α) varies within the range of 10°–30°, and the DOC (h) ranges from 1 to 3 mm. The contact area and contact arc length are calculated based on Eqs. (26) and (27). Table 2 displays the calculated contact area (A), contact arc length (L), contact force (N), and friction force (S_1).

N and S_1 are proposed to be represented by a second order polynomial form, i.e.,

$$f(N) = C_0 + C_1\times\alpha + C_2\times(A\times L) + C_3\times\alpha\times(A\times L) \tag{28}$$

The constants can be determined using polynomial least squares regression techniques based on the data shown in Table 2. Thus, N and S_1 can be expressed as:

$$\begin{aligned} N &= 409.25 + 28.19\alpha + 3.13AL + 0.046\alpha AL,\ R^2 = 0.991 \\ S_1 &= 741.15 - 1.56\alpha + 3.67AL - 0.054\alpha AL,\ R^2 = 0.970 \end{aligned} \tag{29}$$

Thus, submitting Eq. (29) into Eq. (18), the cutting force F_c and normal force F_n can be expressed as:

3.3. Model verification and validation

Table 3 shows the experimental data and model prediction for the cutting force F_c and normal force F_n. It can be seen that the errors of cutting force predicted by model are less than 8.89% and that of normal force are less than 12.81%. The average error of

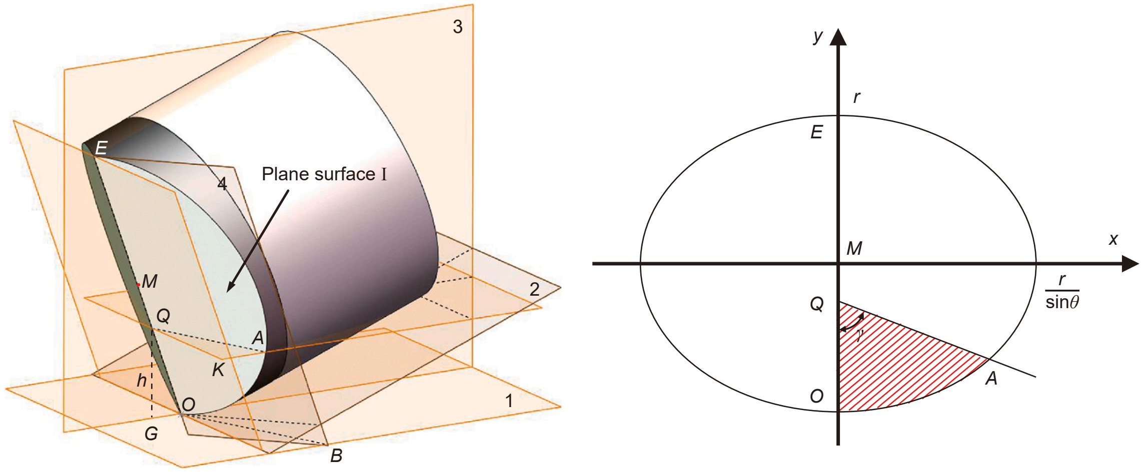

Fig. 10. Schematic diagram of contact area and contact arc length.

Table 2
Calculation results.

No.	α, °	h, mm	A, mm^2	L, mm	N, N	S_1, N
1	10	1.0	5.05	7.84	759.70	749.25
2		1.5	9.31	9.74	1039.45	1032.81
3		2.0	14.30	11.37	1285.28	1297.64
4		2.5	19.89	12.82	1641.79	1502.29
5		3.0	25.98	14.17	1941.51	1770.52
6	15	1.0	5.02	7.73	916.59	770.31
7		1.5	9.32	9.65	1245.62	997.12
8		2.0	14.38	11.29	1520.33	1244.39
9		2.5	20.05	12.76	1873.23	1501.42
10		3.0	26.25	14.12	2188.92	1733.82
11	20	1.0	5.06	7.65	1056.71	761.76
12		1.5	9.45	9.59	1367.51	972.36
13		2.0	14.63	11.26	1669.71	1205.62
14		2.5	20.45	12.76	2113.94	1503.39
15		3.0	26.82	14.14	2482.53	1696.53
16	25	1.0	5.16	7.60	1221.85	773.45
17		1.5	9.69	9.58	1500.52	912.45
18		2.0	15.07	11.28	1867.56	1127.67
19		2.5	21.12	12.81	2364.34	1400.19
20		3.0	27.75	14.22	2767.73	1625.49
21	30	1.0	5.33	7.59	1381.14	721.53
22		1.5	10.08	9.61	1708.97	876.35
23		2.0	15.73	11.35	2105.12	1076.58
24		2.5	22.10	12.91	2584.77	1268.50
25		3.0	29.09	14.36	3053.19	1446.94

Table 3
Comparison of experimental data with calculated values of model.

No.	Experimental data, N		Model prediction, N		Error, %	
	F_c	F_n	F_c	F_n	F_c	F_n
1	1222.33	1737.15	1330.96	1959.66	8.89	12.81
2	1669.77	2391.91	1633.11	2337.44	2.20	2.28
3	2057.53	2998.11	2058.72	2869.57	0.06	4.29
4	2682.19	3523.88	2606.74	3554.75	2.81	0.88
5	3173.94	4155.32	3275.82	4391.30	3.21	5.68
6	1355.68	1958.22	1447.50	2103.85	6.77	7.44
7	1868.05	2565.13	1745.32	2486.08	6.57	3.08
8	2265.88	3183.71	2167.62	3028.09	4.34	4.89
9	2808.30	3861.24	2713.75	3729.04	3.37	3.42
10	3292.25	4472.11	3382.67	4587.57	2.75	2.58
11	1446.61	2147.82	1549.53	2288.31	7.11	6.54
12	1881.29	2754.27	1849.01	2683.44	1.72	2.57
13	2284.45	3397.46	2276.52	3247.48	0.35	4.41
14	2907.96	4258.16	2831.83	3980.14	2.62	6.53
15	3462.20	4870.95	3514.15	4880.37	1.50	0.19
16	1540.62	2425.21	1631.76	2511.19	5.92	3.55
17	1923.59	2910.54	1938.84	2928.96	0.79	0.63
18	2400.86	3608.03	2380.16	3529.36	0.86	2.18
19	3062.70	4518.05	2955.95	4312.71	3.49	4.54
20	3596.73	5264.25	3665.71	5278.32	1.92	0.27
21	1648.64	2618.15	1689.53	2770.57	2.48	5.82
22	2056.42	3211.11	2010.44	3222.87	2.24	0.37
23	2536.02	3950.44	2474.79	3877.35	2.41	1.85
24	3167.25	4758.08	3083.39	4735.12	2.65	0.48
25	3792.67	5531.25	3836.03	5795.93	1.14	4.79

$$
\begin{aligned}
F_c &= 818.50\sin\theta\cos\alpha - 1482.30\sin\alpha + \alpha(56.38\sin\theta\cos\alpha + 3.12\sin\alpha) + AL(6.26\sin\theta\cos\alpha - 7.34\sin\alpha) + \alpha AL(0.092\sin\theta\cos\alpha + 0.108\sin\alpha) \\
F_n &= 818.50\sin\theta\sin\alpha + 1482.30\cos\alpha + \alpha(56.38\sin\theta\sin\alpha - 3.12\cos\alpha) + AL(6.26\sin\theta\sin\alpha + 7.34\cos\alpha) + \alpha AL(0.092\sin\theta\sin\alpha - 0.108\cos\alpha)
\end{aligned}
\tag{30}
$$

cutting force and normal force is 3.13% and 3.68% respectively. This indicates that the precision of the mechanical model for predicting the cutting force and normal force of RDE cutter is very high. In the following, we will analyze the force response of the RDE cutter under different conditions based on this model.

4. Discussion of force responses

4.1. The effect of DOC

Fig. 11 shows the variation laws of experimentally measured and model-predicted cutting force and normal force with the change in DOC. The data points obtained from experimental

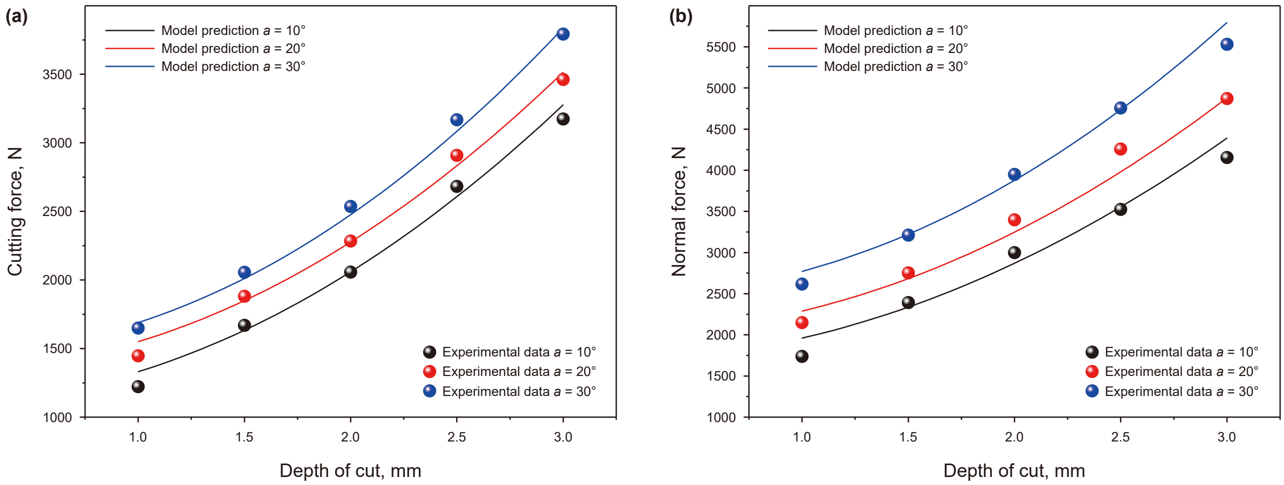

Fig. 11. The variation of cutting force and normal force with DOC.

measurements are basically located on the model-predicted cutting force and normal force variation curves. This reflects that the model established in this paper has a high level of accuracy. In addition, it can be found that with an increase in DOC, cutting force and normal force significantly increase, and the trend is the same under different back rake angle. When the DOC increases from 1.0 to 3.0 mm for back rake angle of 10°, 20° and 30°, the cutting force increases by 1944.92, 1964.81 and 2146.85 N respectively, and normal force increases by 2431.71, 2592.30 and 3025.84 N respectively. When the DOC is small, the volume of broken rock is small. With the increase of DOC, the volume of broken rock increases, and the input energy increases, resulting in the increase of both cutting force and normal force (Lin et al., 2019; Zou et al., 2022). This means that the increase of the DOC will lead to the increase of the force of the RDE, which will lead to the large weight on bit (WOB) and drilling torque value of the PDC bit when the rock is broken at the bottom of the well, resulting in the wear and impact damage of the RDE. Therefore, in the actual drilling, it is necessary to protect the PDC drill bit by controlling the penetration depth of PDC cuter, so that the drill bit can have a long life while breaking the rock efficiently.

Furthermore, by nonlinear fitting analysis, it can be found that the cutting force and the normal force increase with DOC in a quadratic polynomial relationship as shown in Table 4. The slope of the tangent line to the curve can be obtained by taking the derivative, which can be expressed as: $y' = kx + b$. The values of k are larger than zero. This clearly indicates that the rate of increase for the cutting force and normal force gradually accelerates. This change rule can be explained by the theoretical model derived above. According to Eq. (30), the cutting force and normal force increase linearly with $A \times L$ when the rake angel α and ridge angle 2θ are constant. The value of $A \times L$ is calculated by the data in Table 4. Fig. 12 presents the influence of DOC on $A \times L$. It is clearly shown that regardless of how the back rake angle changes, the value of $A \times L$ always significantly increase with the increase in DOC. And it is also in accordance with the increasing quadratic function relationship. Thus, the cutting force and normal force increase with DOC in a quadratic polynomial relationship. This results are also constant with the experimental results for RDE cutter breaking granite obtained by Shao et al. (2021).

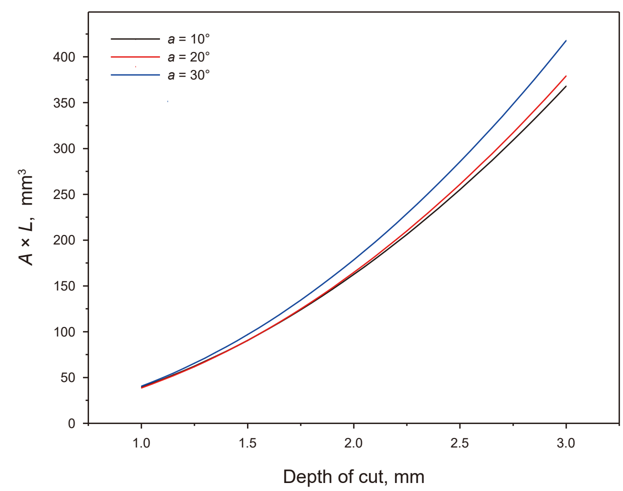

Fig. 12. The product of contact area (A) and contact arc length (L) variation with DOC.

4.2. The effect of back rake angle

In the design of PDC drill bits, the back rake angle typically ranges between 10° and 30°. As illustrated in Fig. 13, both the cutting force and normal force exhibit a gradual increase with the back rake angle, albeit at a relatively slow rate. Specifically, when the back rake angle is increased from 10° to 30° for DOC of 1, 2, and 3 mm, the cutting force rises by 358.60, 416.22, and 560.53 N, respectively, while the normal force increases by 811.00, 1008.04, and 1405.13 N, respectively. Notably, the normal force

Table 4
The results of nonlinear fitting analysis.

α, °	F_c, N	F_n, N	F_c', N	F_n', N
10	$F_c = 244.69h^2 - 5.72h + 1091.7$	$F_n = 305.93h^2 - 7.15h + 1660.2$	$F_c' = 489.38h - 5.72$	$F_n' = 611.86h - 7.15$
20	$F_c = 255.37h^2 - 38.83h + 1333.1$	$F_n = 336.93h^2 - 51.23h + 2002.5$	$F_c' = 510.74h - 38.83$	$F_n' = 673.86h - 51.23$
30	$F_c = 288.08h^2 - 79.05h + 1481.1$	$F_n = 406.03h^2 - 111.41h + 2476.5$	$F_c' = 576.16h - 79.05$	$F_n' = 812.06h - 111.41$

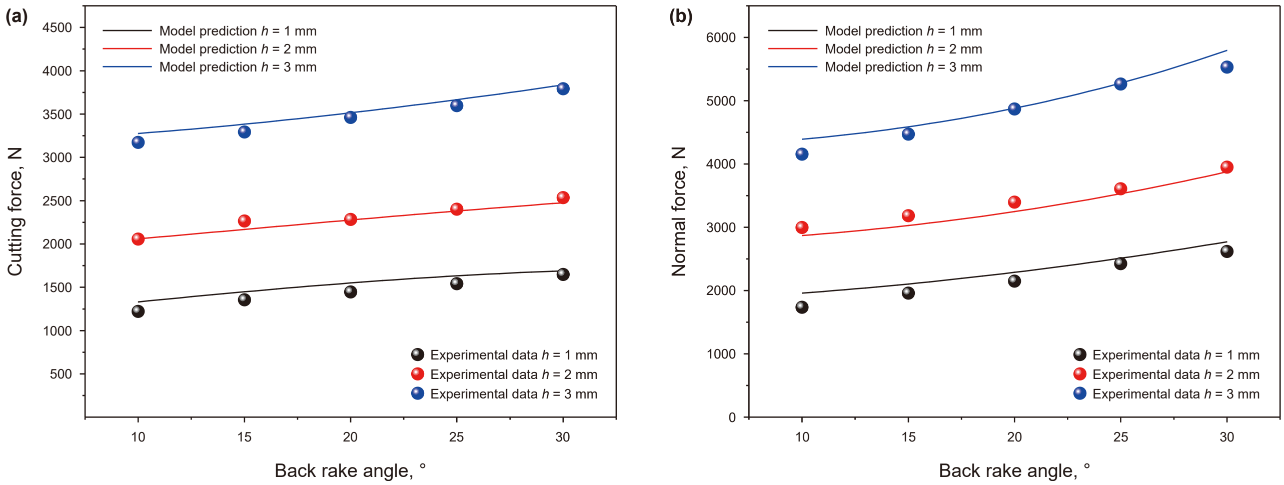

Fig. 13. The variation of cutting force and normal force with back rake angle.

demonstrates a more pronounced sensitivity to changes in the back rake angle compared to the cutting force, a finding that aligns with prior numerical simulations (Gong et al., 2022). The normal force, when aggregated or equivalently distributed, can be used to estimate the overall WOB, whereas the cutting force, when integrated over the drill bit radius, contributes to the calculation of the total torque. Consequently, the measured normal and cutting forces in single-cutter tests serve as reliable indicators of the WOB and drilling torque in actual drilling operations. An increase in the back rake angle leads to a higher WOB, which in turn elevates the resistance encountered during rock penetration and may adversely affect drilling efficiency. Therefore, it is advisable to minimize the back rake angle in drill bit design to optimize performance.

4.3. The effect of cutter diameter

In the current oil and gas drilling industry, the diameters of RDE cutters used in PDC drill bits are predominantly available in three standard sizes: 13, 16, and 19 mm. Building upon the mechanical model of RDE-rock interaction established in Section 3, this study investigates the influence of cutter diameter within the 10–20 mm range on the force response during granite breakage by RDE cutters. As demonstrated in Fig. 14, both the cutting force and normal force exhibit a substantial increase with larger RDE diameters, with this trend becoming particularly pronounced at greater DOC. For example, at a DOC of 3 mm, increasing the RDE diameter from 10 to 20 mm results in a 48.60% increase in cutting force (1318.13 N) and a 45.50% increase in normal force (1739.10 N).

Furthermore, we calculated the product of contact area (A) and contact arc length (L) across different cutter diameters, as illustrated in Fig. 15. The results indicate that cutter diameter has a significant influence on the $A \times L$ value, with its variation pattern closely resembling the force response during RDE rock breakage, showing an essentially linear increase. Notably, the rate of increase becomes more rapid with greater DOC values. According to Eq. (30), when all other parameters remain constant, both cutting force and normal force exhibit a linear relationship with $A \times L$. Given that Fig. 15 demonstrates a linear increase in $A \times L$ with cutter diameter, it logically follows that the cutting force and normal force also increase linearly with cutter diameter. In PDC bit design, the selection of PDC cutter size is crucial. While using smaller-diameter PDC cutters can effectively reduce the load on individual cutters, minimize impact damage risks, and thereby extend the overall bit life, it leads to an increased number of cutters on the bit. This, in turn, weakens the bit's ability to penetrate the formation, which is not conducive to improving the ROP. Therefore, the selection of PDC

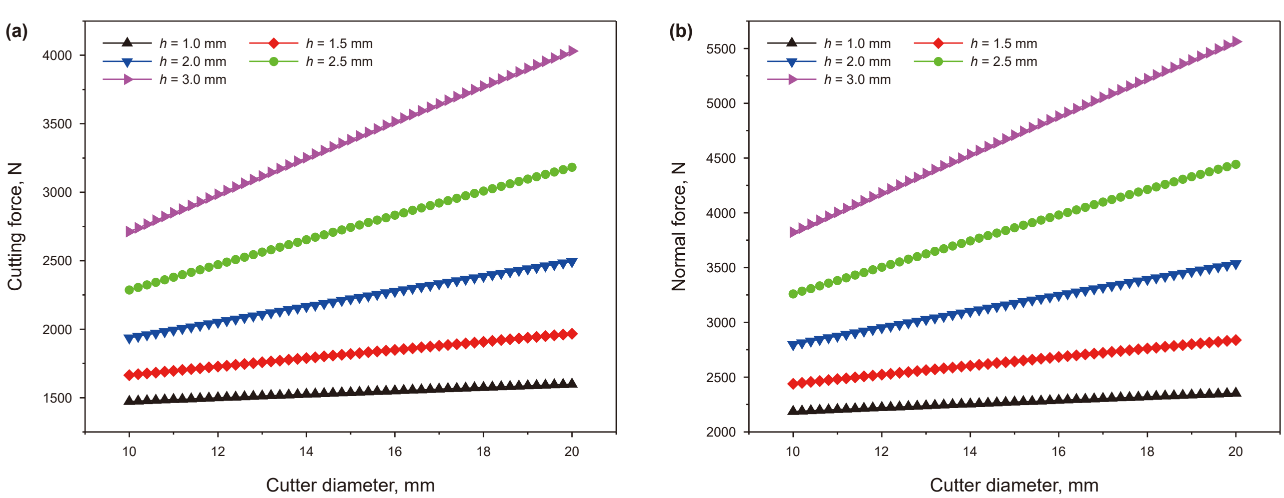

Fig. 14. The variation of cutting force and normal force with cutter diameter.

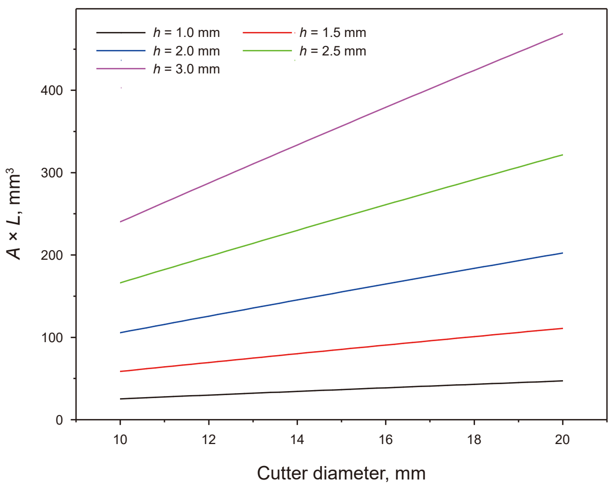

Fig. 15. The product of contact area (A) and contact arc length (L) variation with cutter diameter.

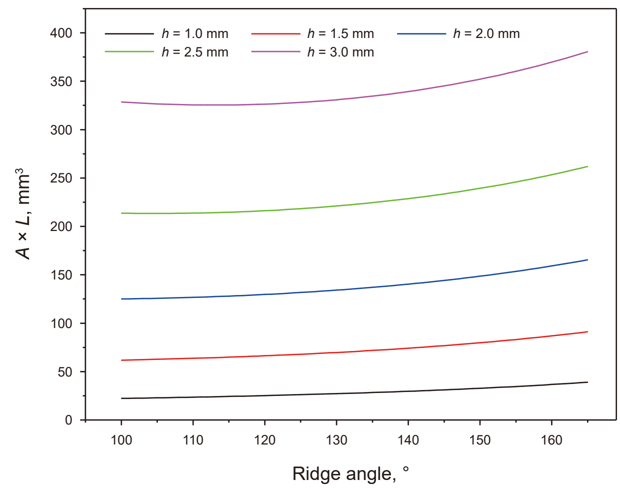

Fig. 17. The product of contact area (A) and contact arc length (L) variation with ridge angle.

cutter size requires a comprehensive trade-off between the two key performance indicators: bit life and ROP.

4.4. The effect of ridge angle

The ridge angle is a crucial geometric parameter of the RDE cutter. It directly determines the direction of contact force and friction force between the cutter and rock, thereby affecting the magnitude of cutting force and normal force (Fig. 7). Currently, the commonly used range of ridge angle in the oil and gas drilling industry is 100°–165°. Therefore, in this section, based on the mechanical model of RDE-rock interaction established in Section 3, the variation of cutting force and normal force as the ridge angle in the range of 100°–165° are studied. As shown in Fig. 16, with the increase in ridge angle, the cutting force and normal force show an increasing trend. Moreover, with the increase in DOC, the increase in cutting and normal forces becomes more pronounced. However, the rate of increase for each differs slightly, the cutting force increases more rapidly, while the increase in normal force is more gradual. For example, when the DOC is 3 mm, and the ridge angle of RDE increases from 100° to 165°, the cutting force increases by 1276.03 N, and the normal force increases by 750.87 N. During the process of rock fragmentation with a RDE, a shear stress concentration zone forms at the contact point between the rock and the chisel edge, while the ridge surface causes tensile failure of the rock laterally, leading to rock fragmentation under the combined action of shear and tensile forces (Gong et al., 2022; He et al., 2023). When the ridge angle is small, the lateral tensile effect of the ridge surface on the rock is stronger, making the rock more prone to fragmentation under combined shear and tensile forces, resulting in higher rock-breaking efficiency. As the ridge angle increases, the tensile effect of the ridge surface gradually weakens, and shear action becomes the dominant rock-breaking mechanism. When the ridge angle increases to 180°, the RDE degrades into a conventional planar cutter, relying solely on shear for rock breaking. Since the tensile strength of rock is significantly lower than its shear strength (Xiong et al., 2023a), compared to rock breaking via tensile action, relying on shear action makes it more difficult to fragment the rock, requiring greater cutting and normal forces.

Furthermore, Fig. 17 shows the influence of ridge angle on the product of contact area (A) and contact arc length (L). As the ridge angle increases, the value of $A \times L$ generally tends to increase, but

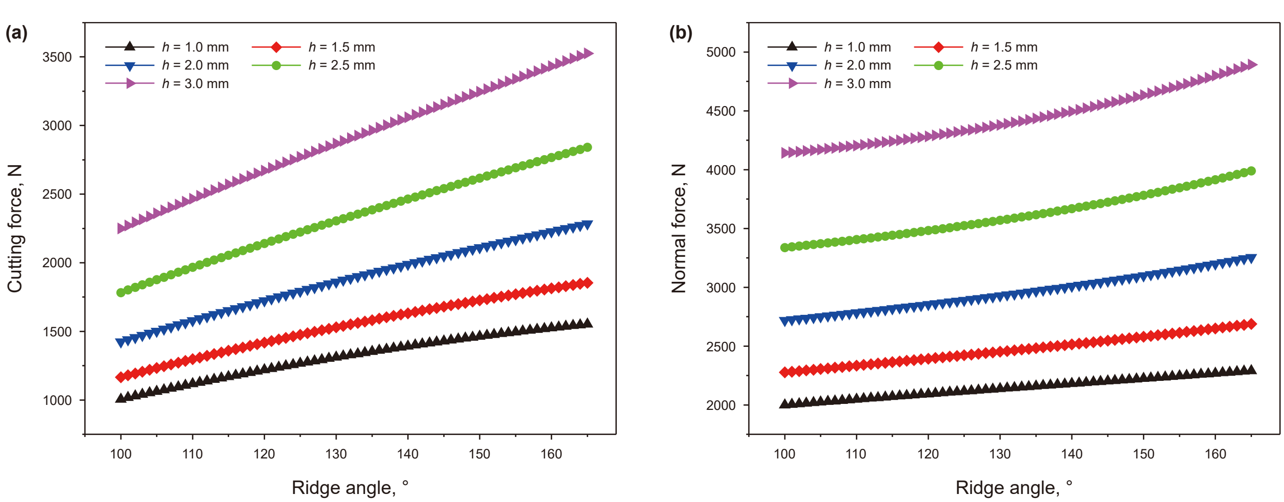

Fig. 16. The variation of cutting force and normal force with ridge angle.

the increase is not very significant. Considering only from the perspective of $A\times L$, the changes in the cutting force and normal force should not be very noticeable. However, as indicated by Eq. (30), the cutting force and normal force are not only positively related to $A\times L$, but also positively related to $\sin\theta$. Therefore, the ridge angle affects the magnitude of cutting force and normal force by altering $A\times L$ and $\sin\theta$.

We know that in the PDC bit design process, to enhance the rock-breaking efficiency, priority should be given to reducing the ridge angle of the RDE. This design strategy can sharpen the cutting edge, thereby improving its ability to penetrate the rock, and achieve more efficient rock-breaking results by optimizing the synergistic effect of shear and tensile forces. However, it should be noted that an excessively small ridge angle can make the cutting edge too sharp, leading to increased wear in hard rock formations, which can significantly shorten the bit's service life. Therefore, when selecting the ridge angle, it is necessary to strike a balance between rock-breaking efficiency and bit durability. By comprehensively evaluating cutting forces, ridge angle effects, and rock mechanical properties, the bit can be ensured to have both high rock-breaking efficiency and a long service life in deep hard rock formation drilling operations.

4.5. Variable importance analysis

Based on above analysis, it is evident that the DOC, back rake angle, cutter diameter, and ridge angle have a significant impact on cutting force and normal force, but the influence degree is different. In order to quantitatively assess the influence degree of these four parameters for cutting force and normal force, the 5×5×5×5 full factorial experiments were designed. The factor—DOC has five levels, i.e., 1.0, 1.5, 2.0, 2.5 and 3.0 mm, the factor—back rake angle has five levels, i.e., 10°, 15°, 20°, 25° and 30°, the factor—cutter diameter has five levels, i.e., 10.0, 12.5, 15.0, 17.5 and 20.0 mm, and the factor—ridge angle has five levels as well, i.e., 100°, 116.25°, 132.5°, 148.75° and 165°. Based on the mechanical model of RDE–rock interaction established in Section 3, the cutting force and normal force of 625 groups with different parameters were calculated.

Random forest (RF) is a commonly-used machine learning algorithm, which combines the output of multiple decision trees to reach a single result (Biau and Scornet, 2016). Its ease of use and flexibility have fueled its adoption, as it handles both classification and regression problems. Variable importance measure is used to calculate the importance of sample features and quantitatively describe the contribution of features to classification or regression. RF can be used to evaluate the importance of features (Palczewska et al., 2014), which is mainly divided into two methods: (1) Mean decrease impurity (MDI), which measures the importance of a node by statistically evaluating the decrease in impurity during node splitting; (2) Mean decrease accuracy (MDA) involves randomly permuting the values of a specific feature in the out-of-bag (OOB) dataset and then re-predicting. The importance of the feature is calculated by measuring the extent to which the accuracy of classification/regression declines. MDI uses the training set data, and the evaluation value of MDI feature importance can be obtained directly after RF training (Li et al., 2019). The MDA uses OOB data and needs to run a feature importance assessment program independently after RF training is complete. Because MDI uses training data entirely, it can affect the accuracy of the assessment and tends to give more weight to high cardinality features. In contrast, the MDA results were more accurate, which has been proven by previous researchers (Biau and Scornet, 2016).

In this part, the MDA method was used to evaluate the influence weights of factors such as DOC, back rake angle, cutter diameter, and ridge angle on cutting force and normal force, based on the 625 groups data. The data is split into 75% for training and 25% for testing. The coefficient of determination (R^2) is used to evaluate the model's fitting accuracy. GridSearchCV is applied for hyperparameter tuning, yielding optimal parameters: n_estimators = 115, max_depth = 12, min_samples_split = 3, max_features = 7, min_samples_leaf = 1. The model achieves an R^2 of 0.935 on the test set, demonstrating high accuracy.

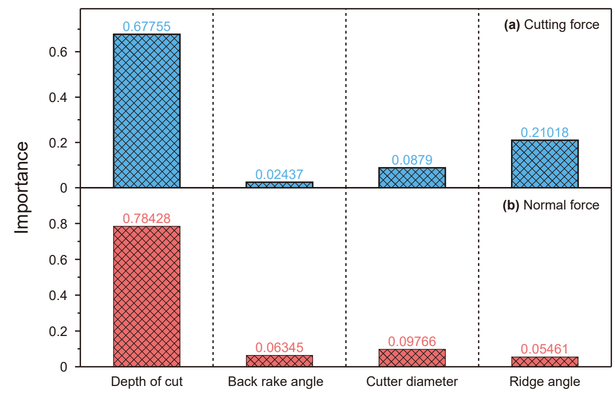

Fig. 18. The influence weight of different parameters on cutting force and normal force.

The influence weight of j (the j dimension of the sample) can be calculated as follows:

$$\mathrm{MDA}_r(j)=\frac{1}{T}\sum_t^T\left[\frac{1}{|D_t|}\left(\sum_{X_i^j\in D_t^j}\sum_k\left(R_k\left(X_i^j\right)-y_i^k\right)^2-\sum_{X_i\in D_t}\sum_k\left(R_k(X_i)-y_i\right)^2\right)\right] \tag{31}$$

where, T is the number of random trees in RF, (X_i, y_i) is the sample, X_i^j is a sample obtained by randomly swapping the j dimension (feature) of X_i, D_t is the out-of-bag (OOB) sample set for a random tree t, D_t^j is the sample set formed after j dimensional exchange, y_i^k represents the k dimensional output.

Fig. 18 shows the influence weights of DOC, back rake angle, cutter diameter and ridge angle on cutting force and normal force respectively. It can be seen that among these four parameters, the influence weight of DOC is the largest. In comparison, the influence weights of back rake angle, cutter diameter, and ridge angle are much less. In addition, it can be observed that the influence weight of the ridge angle on the cutting force is much greater than its influence weight on the normal force. The influence weight of the cutter diameter on cutting force and normal force is close, and the influence weight of the back rake angle on the cutting force is less than its influence weight on the normal force. For the cutting force, the ranking of the influence weight of the four parameters from high to low is: DOC, ridge angle, cutter diameter, and back rake angle; while for the normal force, the ranking of influence weight from high to low is: DOC, cutter diameter, back rake angle, and ridge angle.

5. Conclusions

In this paper, a series of single cutter tests on granite by RDE were conducted, and the triaxial forces under different DOC and back rake angle were measured. The first mechanical model of interaction between RDE and rock was established through theoretical derivation. The influence of DOC, back rake angle, cutter diameter and ridge angle on cutting force and normal force was analyzed. The following conclusions are drawn from the studies.

(1) The established mechanical model for predicting the cutting force and normal force of RDE cutter has high precision. The average error of cutting force and normal force is 3.13% and 3.68% respectively.
(2) The cutting force and the normal force increase with DOC in a quadratic polynomial relationship and the increase trend is the same under different back rake angle. Actual drilling requires controlling PDC cutter penetration depth to protect the bit, ensuring efficient rock breaking and extended bit life.
(3) The cutting force and normal force increase with the increase in back rake angle, but the rate of increase is relatively slow. It is advisable to minimize the back rake angle in drill bit design to optimize performance.
(4) The cutting force and normal force significantly increase as the diameter of RDE increases, especially when the DOC is larger, the trend of increase is more evident. The selection of PDC cutter size requires a comprehensive trade-off between the two key performance indicators: bit life and ROP.
(5) With the increase in ridge angle, the cutting force and normal force show an increasing trend. To improve rock-breaking efficiency, the ridge angle can be reduced, but wear resistance must be considered.
(6) The influence weight of DOC on cutting force and normal force is the largest, and the influence weights of back rake angle, cutter diameter, and ridge angle are much less.

This paper focuses on the mechanical analysis of RDE PDC cutters, investigating the influence of structural and drilling parameters on their loading behavior, and provides recommendations for parameter selection. However, the analysis considers only drill bit loading, without accounting for PDC cutter life. Therefore, further research is needed on the impact resistance and wear resistance of RDE cutters to comprehensively evaluate rock-breaking performance and durability, ultimately establishing specific recommended values for bit structure and operating parameters.

CRediT authorship contribution statement

Chao Xiong: Writing – original draft, Methodology, Investigation, Conceptualization. **Xin-Long Li:** Writing – review & editing, Investigation, Data curation. **Sen-Lin He:** Writing – review & editing, Methodology, Investigation, Formal analysis. **Zhong-Wei Huang:** Funding acquisition, Conceptualization. **Huai-Zhong Shi:** Resources, Conceptualization. **Wen-Hao He:** Writing – review & editing, Methodology, Investigation.

Conflict of interest

None.

Acknowledgements

This work was supported by the Innovative Research Group Project of National Natural Science Foundation of China (No. 5241002), the National Natural Science Foundation of China (No. 52304014), the Science Foundation of China University of Petroleum, Beijing (2462025YJRC025), and Research Project of China National Petroleum Corporation Science and Technology Innovation Fund (No. 2024DQ02-0147).

References

Bellin, F., Dourfaye, A., King, W., et al., 2010. The current state of PDC bit technology. World Oil 231 (9), 41–46.
Biau, G., Scornet, E., 2016. A random forest guided tour. Test 25, 197–227.
Che, D., Ehmann, K., 2014. Experimental study of force responses in polycrystalline diamond face turning of rock. Int. J. Rock Mech. Min. Sci. 72, 80–91. https://doi.org/10.1016/j.ijrmms.2014.08.014.
Che, D., Zhang, W., Ehmann, K., 2017. Chip formation and force responses in linear rock cutting: an experimental study. J. Manuf. Sci. Eng. 139 (1), 011011. https://doi.org/10.1115/1.4033905.
Chen, P., Miska, S., Yu, M., et al., 2021. Modeling of cutting rock: From PDC cutter to PDC bit—modeling of PDC bit. SPE J. 26 (6), 3465–3487. https://doi.org/10.2118/206725-PA.
Chen, P., Miska, S.Z., Ren, R., et al., 2018. Poroelastic modeling of cutting rock in pressurized condition. J. Petrol. Sci. Eng. 169, 623–635. https://doi.org/10.1016/j.petrol.2018.06.009.
Cheng, Z., Li, G.S., Huang, Z.W., et al., 2019. Analytical modelling of rock cutting force and failure surface in linear cutting test by single PDC cutter. J. Petrol. Sci. Eng. 177, 306–316. https://doi.org/10.1016/j.petrol.2018.09.023.
Crane, D., Zhang, Y., Douglas, C., et al., 2017. Innovative PDC cutter with elongated ridge combines shear and crush action to improve PDC bit performance. In: SPE Middle East Oil & Gas Show and Conference. https://doi.org/10.2118/183984-MS.
Dai, X.W., Huang, Z.W., Shi, H.Z., et al., 2023. Experimental investigation on the cuttings formation process and its relationship with cutting force in single PDC cutter tests. Pet. Sci. 20 (3), 1779–1787. https://doi.org/10.1016/j.petsci.2022.10.021.
Fu, X.K., Xiong, C., Shi, H.Z., et al., 2025. Comparative analysis of rock breakage characteristics and failure mode on conventional and conical PDC cutter cutting carbonate. Pet. Sci. 22 (2), 821–834. https://doi.org/10.1016/j.petsci.2024.12.016.
Gerbaud, L., Menand, S., Sellami, H., 2006. PDC bits: All comes from the cutter/rock Interaction. In: IADC/SPE Drilling Conference. https://doi.org/10.2118/98988-MS.
Glowka, D.A., 1989. Use of single-cutter data in the analysis of PDC bit designs: Part 1-development of a PDC cutting force model. J. Petrol. Technol. 41 (8), 797–849. https://doi.org/10.2118/15619-PA.
Gong, J., Wu, W., Zhou, Z., 2022. Numerical simulation on rock-breaking mechanism of axe-shaped cutter. China Petroleum Machinery 50 (9), 44–51. https://doi.org/10.16082/j.cnki.issn.1001-4578.2022.09.006 (in Chinese).
Gumich, D., Pak, M., Lomov, A., et al., 2017. New ridge diamond elements improve PDC bit efficiency. In: SPE Russian Petroleum Technology Conference. https://doi.org/10.2118/187717-MS.
He, W, Zhang, R, Liu, L, et al., 2023. Numerical simulation of rock-breaking mechanisms by triple-ridged PDC cutter in hard rocks. Geoenergy Science and Engineering 229, 212148. https://doi.org/10.1016/j.geoen.2023.212148.
Li, W., Ling, X., Pu, H., 2020. Development of a cutting force model for a single PDC cutter based on the rock stress state. Rock Mech. Rock Eng. 53 (1), 185–200. https://doi.org/10.1007/s00603-019-01893-7.
Li, X., Wang, Y., Basu, S., et al., 2019. A debiased MDI feature importance measure for random forests. Adv. Neural Inf. Process. Syst. 32. https://doi.org/10.48550/arXiv.1906.10845.
Lin, Z., Yang, Y., Yu, H., et al., 2019. Study on the rock-breaking efficiency of ridge cutter. Chin. J. Undergr. Space Eng. 15, 751–772. https://doi.org/10.20174/j.juse.2019.s2.034 (in Chinese).
Liu, Z., Zhao, H., Li, J., et al., 2022. Study on cuttings generated by ridge cutter. Oil Field Equipment 51 (4), 12–21 (in Chinese).
Lomov, A., James, B., Konysbekuly, G., et al., 2018. The combination of ridge and conical elements is a new approach for drilling out hard carbonates and sandstones without drop in ROP. In: SPE Russian Petroleum Technology Conference. https://doi.org/10.2118/191522-18RPTC-MS.
Ma, Q., Wang, R., 2006. Experimental study on force of PDC cutter breaking rock. Journal of China University of Petroleum 30 (2), 45–47+58 (in Chinese).
Miyazaki, K., Ohno, T., Karasawa, H., et al., 2019. Performance of polycrystalline diamond compact bit based on laboratory tests assuming geothermal well drilling. Geothermics 80, 185–194. https://doi.org/10.1016/j.geothermics.2019.03.006.
Negm, S., Aguib, K., Karuppiah, V., et al., 2016. The disruptive concept of 3D cutters and hybrid bits in polycrystalline diamond compact drill-bit design. In: Abu Dhabi International Petroleum Exhibition & Conference. https://doi.org/10.2118/183335-MS.
Nishimatsu, Y., 1972. The Mechanics of Rock Cutting. International Journal of Rock Mechanics and Mining Sciences & Geomechanics Abstracts. Elsevier, pp. 261–270.
Palczewska, A., Palczewski, J., Marchese, Robinson R., et al., 2014. Interpreting random forest classification models using a feature contribution method. Bouabana-Tebibel, T., Rubin, S. (Eds.), Integration of Reusable Systems. Advances in Intelligent Systems and Computing, vol. 263. Springer, Cham. https://doi.org/10.1007/978-3-319-04717-1_9.

Schlumberger, 2026. Axeblade Ridged Diamond Element Bit. https://www.slb.com/products-and-services/innovating-in-oil-and-gas/drilling/bottomhole-assemblies/drill-bits/blade-family-bits/axeblade-ridged-diamond-element-bit.

Shao, F., Liu, W., Gao, D., et al., 2021. Study on rock-breaking mechanism of axe-shaped PDC cutter. J. Petrol. Sci. Eng. 205, 108922. https://doi.org/10.1016/j.petrol.2021.108922.

Shi, H.Z., He, S.L., Xiong, C., et al., 2026. Development and application of a hybrid PDC bit for drilling the high temperature granite formation in the deep geothermal exploration well Fushenre-1. Energy Geoscience 7 (3), 100467. https://doi.org/10.1016/j.engeos.2025.100467.

Xiong, C., Dai, X.W., Shi, H.Z., et al., 2020a. Investigation on rock breakage mechanism of stinger PDC cutter and hybrid cutter arrangement design. In: 54th US Rock Mechanics/Geomechanics Symposium. ARMA-2020-1419.

Xiong, C., Huang, Z.W., Shi, H.Z., et al., 2023a. Performances of a stinger PDC cutter breaking granite: Cutting force and mechanical specific energy in single cutter tests. Pet. Sci. 20 (2), 1087–1103. https://doi.org/10.1016/j.petsci.2022.10.006.

Xiong, C., Huang, Z.W., Shi, H.Z., et al., 2023b. Investigations on the stinger PDC cutter breaking granitoid under in-situ stress and hydrostatic pressure conditions. Int. J. Rock Mech. Min. Sci. 164, 105312. https://doi.org/10.1016/j.ijrmms.2022.105312.

Xiong, C., Huang, Z.W., Shi, H.Z., et al., 2021. 3D cutting force model of a stinger PDC cutter: Considering confining pressure and the thermal stress. Rock Mech. Rock Eng. 54, 5001–5022. https://doi.org/10.1007/s00603-021-02494-z.

Xiong, C., Huang, Z.W., Yang, R.Y., et al., 2020b. Comparative analysis cutting characteristics of stinger PDC cutter and conventional PDC cutter. J. Petrol. Sci. Eng. 189, 106792. https://doi.org/10.1016/j.petrol.2019.106792.

Zhao, R., Chen, Z., Shi, H., et al., 2021. Numerical simulation study on characteristics of tight hard sand broken by axe-shaped PDC cutter. China Petroleum Machinery 49 (10), 8–16. https://doi.org/10.16082/j.cnki.issn.1001-4578.2021.10.002 (in Chinese).

Zhu, X.H., Luo, Y.X., Liu, W.J., et al., 2022. Rock cutting mechanism of special-shaped PDC cutter in heterogeneous granite formation. J. Petrol. Sci. Eng. 210, 110020. https://doi.org/10.1016/j.petrol.2021.110020.

Zou, D., Chen, Y., Zhao, F., et al., 2021a. Study on rock breaking rules of axe-shaped PDC cutter with numerical simulation. Special Oil Gas Reservoirs 28 (6), 137–143 (in Chinese).

Zou, D., Pan, L., Cui, Y., et al., 2022. Rock breaking mechanism and experimental study of axe-shaped PDC cutter. China Petroleum Machinery 50 (1), 34–40. https://doi.org/10.16082/j.cnki.issn.1001-4578.2022.01.005 (in Chinese).

Zou, D., Ren, Z., Chen, Y., et al., 2021b. Experimental study on PDC cutter profile optimization for siliceous dolomite. Drill. Prod. Technol. 44 (6), 19–24 (in Chinese).